Available online at www.sciencedirect.com
ScienceDirect
Journal of the European Ceramic Society 28 (2008) 2589–2596
www.elsevier.com/locate/jeurceramsoc

Effects of milling condition on the formation of core–shell structure in $BaTiO_3$ grains

Chang-Hoon Kim [a,*], Kum-Jin Park [a], Yeo-Joo Yoon [b], Dong-Sook Sinn [a], Young-Tae Kim [a], Kang-Heon Hur [c]

[a] *Material Development Group, LCR Division, Samsung Electro-Mechanics Co., Ltd., Suwon, Republic of Korea*
[b] *Analytical Research Group, Central R&D Institute, Samsung Electro-Mechanics Co., Ltd., Suwon, Republic of Korea*
[c] *LCR Development Team, LCR Division, Samsung Electro-Mechanics Co., Ltd., Suwon, Republic of Korea*

Received 5 January 2008; received in revised form 17 March 2008; accepted 28 March 2008
Available online 16 May 2008

Abstract

The effects of ball-milling condition on the formation of core–shell structure in $BaTiO_3$ grains were studied. As the ball-milling time increased from 12 h to 48 h, the stress given by the milling process was accumulated in the powders while the primary powder size was reduced at 24 h milling and additional comminution of powders occurred at 48 h milling. The change of powder characteristics did not induce any difference in the sinterability but influenced on the formation of core–shell structure. The increase in milling time facilitated the shell formation leading to the increased shell portion in the core–shell grain. And at 48 h milling, the comminution effect as well as the increased milling stress resulted in the extensive formation of shell which was reflected by the remarkable rise of low temperature part of relative dielectric constant vs. temperature curve.

Keywords: Milling; $BaTiO_3$; Core–shell

1. Introduction

Recent demand for a thin dielectric layer less than 1 μm for high-capacitance and small-size multilayer ceramic capacitor (MLCC) development requires precise control of microstructure consisting of dielectric grains in about 200 nm sizes. To reduce the temperature dependence of capacitance over a wide temperature range and achieve a reliable performance under the increased electric field intensity applied to the thin dielectric layer, a well defined 'core–shell' structure in the individual $BaTiO_3$ (BT) grains needs to be formed.[1] In such a core–shell structure, the additive elements are partially dissolved in BT lattice to form a shell which surrounds the core region. The shell is known to have nonferroelectric pseudocubic structure, whereas the core is pure BT with a ferroelectric tetragonal structure.[2–5]

The most important in understanding of the core–shell structure is the role of additive elements in the shell formation. It seems like that rare-earth elements play a dominant role in the shell formation, as reported in various studies about the mechanism of core–shell formation including our previous research.[6–11] In addition to the material aspect, i.e., the proper composition of additives, process conditions for MLCC fabrication also can have influence on the core–shell formation. Although the sintering parameters such as soak temperature and atmosphere are of significance in controlling the microstructure of MLCC, the physical, chemical, or mechanical properties of starting powders could also have a significant effect on it. Previously, it has been reported that as the BT and additive powders were ball-milled for a longer time, the plot of capacitance change with temperature of the sintered ceramic sample had more negative ends on both of cold and hot temperature sides in spite of increased room temperature dielectric constant.[12] The study of the effects of ball-milling condition on the chip microstructure showed that the relative fractions of dielectric grains having core, shell, and core–shell structures were varied depending on milling condition.[13,14] This observation, however, seems to be insufficient to clearly understand how the milling condition could affect the extent of shell formation.

* Corresponding author.
E-mail address: ch1221.kim@samsung.com (C.-H. Kim).

0955-2219/$ – see front matter © 2008 Elsevier Ltd. All rights reserved.
doi:10.1016/j.jeurceramsoc.2008.03.030

In the present study, ball-milling time was selected as a process parameter to affect the core–shell formation. After ball-milling for a different time, the powders were characterized in terms of size distribution and residual strain. And, the microstructure and dielectric property of sintered samples using those powders were investigated, aiming at understanding the relationship between ball-milling condition and the core–shell structure.

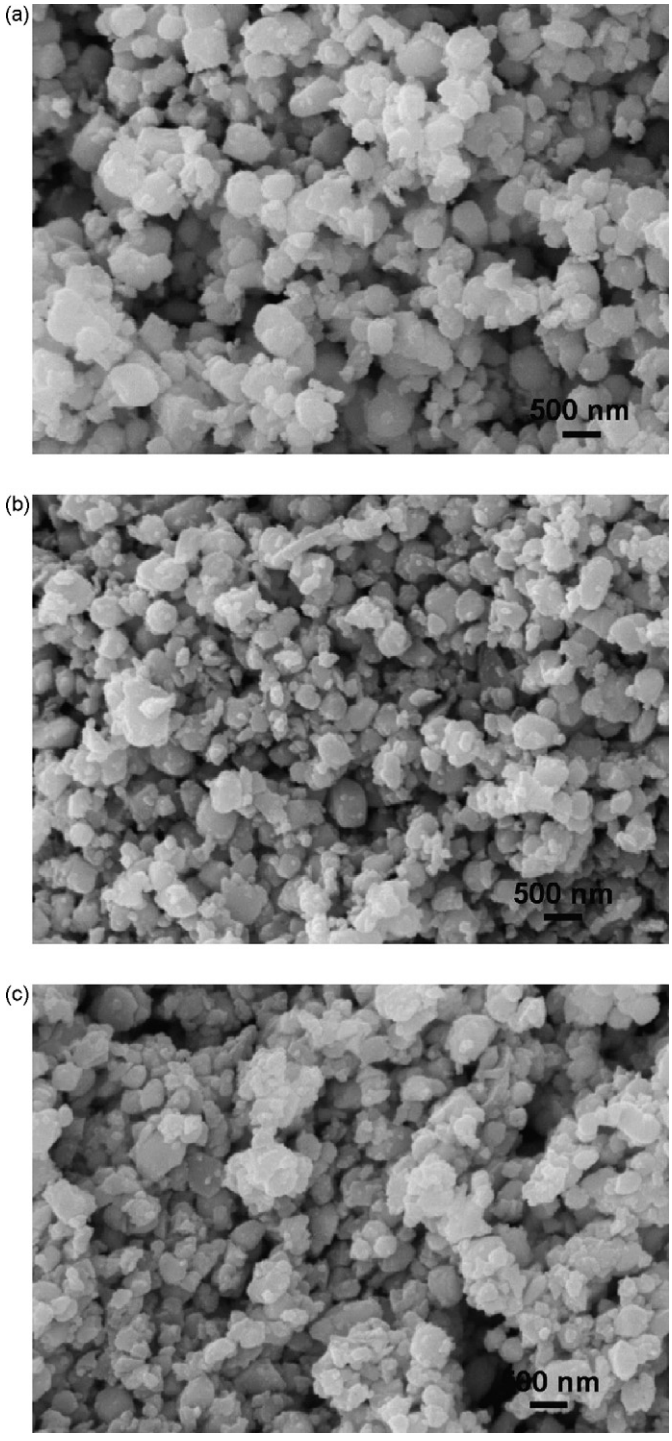

Fig. 1. Scanning electron micrographs of powders after ball-milling for (a) 12 h, (b) 24 h, (c) 48 h.

2. Experimental procedure

In our previous study, BT specimens added with different amounts of Y and Mg were prepared, and their microstructures were investigated to understand the formation mechanism of core–shell structure.[11] Among the various compositions, BT specimen with 3.6 mol% Y and 1.8 mol% Mg was turned out to have a well-developed core–shell structure, so it was subject to the experiments for the investigation of the effects of ball-milling time on the core–shell formation.

To fabricate the specimen of the above-mentioned composition, hydrothermally synthesized BT powders of 400 nm nominal size (Sakai Chemical Industry, Sakai, Japan) were weighed with 1.4 wt% $MgCO_3$ (Kyorix, Nagoya, Japan), 0.9 wt% Y_2O_3 (Rhodia, Paris, France), 2.0 wt% $BaCO_3$ (Sakai Chemical), and 0.6 wt% SiO_2 (Kojundo Chemical, Sakado, Japan) powders. The $BaCO_3$ and SiO_2 were added as sintering aids. The powders were ball-milled in water with dispersant for a different time; 12 h, 24 h and 48 h. After ball-milling, the mixed powders were dried at 120 °C, granulated with polyvinyl alcohol, and pressed uniaxially into a disk of 15 mm diameter. The disks were baked at 400 °C for binder removal and annealed at 700 °C for 1 h, to be mechanically robust during the following processes. The specimens were sintered at 1350 °C for 2 h, in N_2–H_2–H_2O atmosphere ($P_{O_2} \sim 10^{-9.3}$ atm).

To estimate size distribution, both powders and sintered samples were observed using scanning electron microscope (SEM) (S440, Leica, Cambridge, UK). Prior to SEM investigation, the samples were polished down to 0.3 μm grade and chemically etched to distinguish individual grains. And, the powders were characterized by laser scattering particle size analysis (PSA) (LA-910, Horiba, Kyoto, Japan) and surface area analysis (HM Model-1208, Mountech Co., Tokyo, Japan). Bulk density of sintered samples was measured by Archimedes method.

The structural changes of milled powders were investigated by X-ray diffraction (XRD) (RINT 2200HF, Rigaku, Tokyo, Japan) and Raman spectroscopy (RM 2000 series, Renishaw,

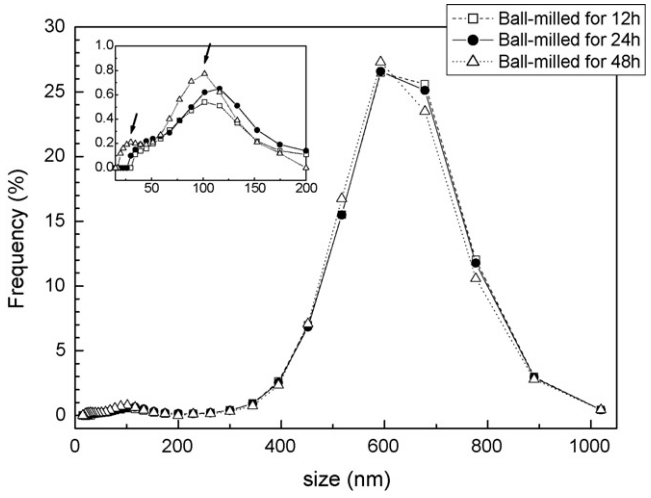

Fig. 2. Particle size distribution of the powders ball-milled for 12 h, 24 h and 48 h, which was measured by laser scattering method; the inserted plot is a magnified portion of the curves up to 200 nm range.

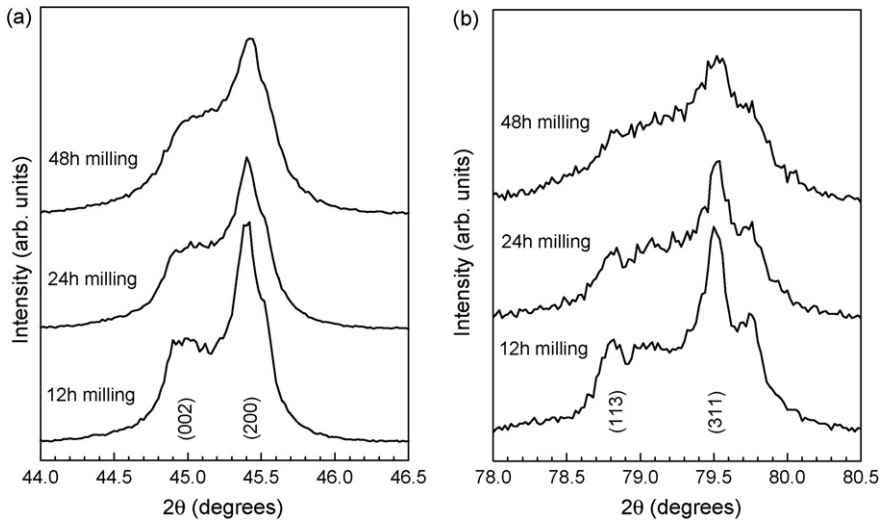

Fig. 3. XRD patterns of the powders after ball-milling for a different time; (a) (0 0 2)/(2 0 0), (b) (1 1 3)/(3 1 1) peaks.

Gloucestershire, UK). The XRD measurements were carried out with Cu K_α radiation in the 2θ range of 44° to 46.5°, covering (0 0 2) and (2 0 0) peaks of tetragonal BT, at 0.02° step. The core–shell grains in the sintered samples were investigated by differential scanning calorimetry (DSC) (DSC7, PerkinElmer, Waltham, MA) and transmission electron microscopy (TEM). DSC measurements were performed up to 150 °C in N_2 atmosphere to check a tetragonal to cubic transition peak at about 125 °C, the integrated intensity of which corresponds to the proportion of the tetragonal core region. TEM samples were prepared using tripod polishing followed by ion beam thinning (PIPS, Gatan, Pleasanton, CA), and investigated using Tecnai G2 F20 microscope (FEI, Hillsboro, OR) operating at 200 kV.

For the measurement of dielectric properties of the specimen, both surfaces of the sintered samples were coated with InGa paste. The capacitance of the disk was measured in the temperature range of −15 °C to 145 °C at 1 kHz, $1V_{rms}$ using 4284A (Agilent Technologies, Santa Clara, CA) precision LCR meter.

3. Results and discussion

3.1. Characteristics of powders

Fig. 1 shows SEM images of the powders ball-milled for 12 h, 24 h and 48 h, respectively. Since the powders of BT and addi-

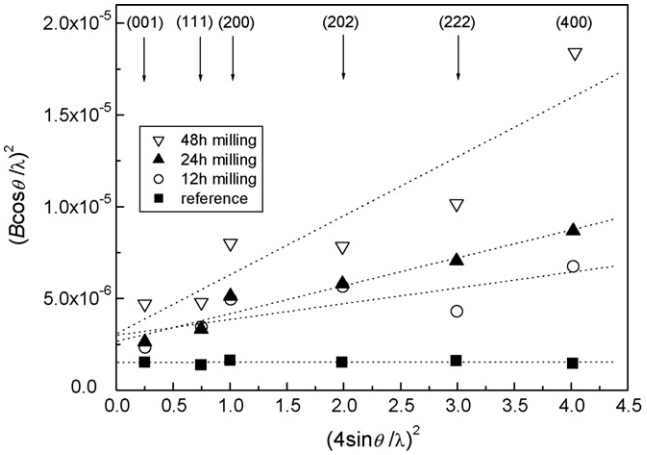

Fig. 4. Hall–Williamson plots determined from (0 0 1), (1 1 1), (2 0 0), (2 0 2), (2 2 2), (4 0 0) peaks of the powders milled for a different time.

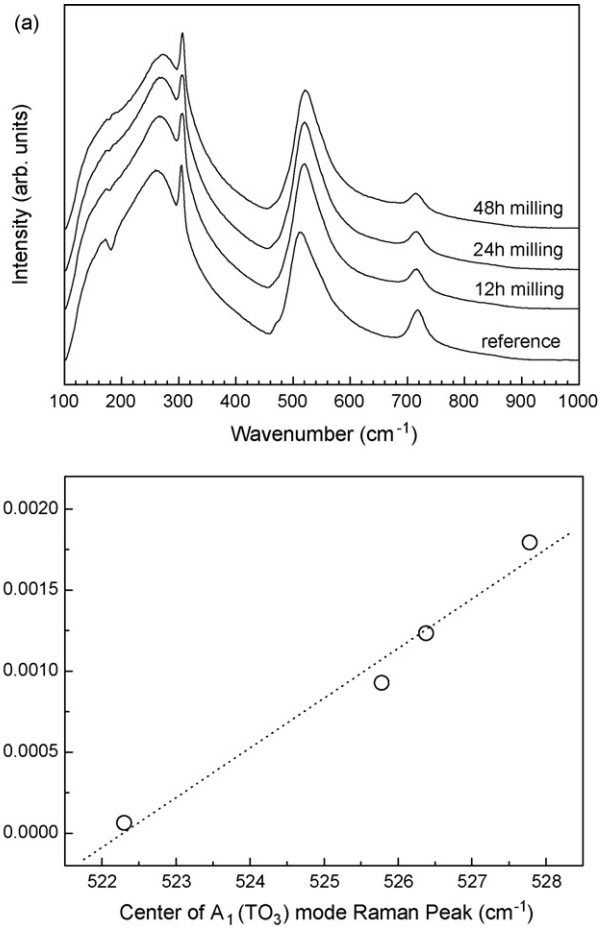

Fig. 5. (a) Raman spectra of powders ball-milled for a different time, (b) plot of XRD strain vs. $A_1(TO_3)$ Raman peak position for the ball-milled powders.

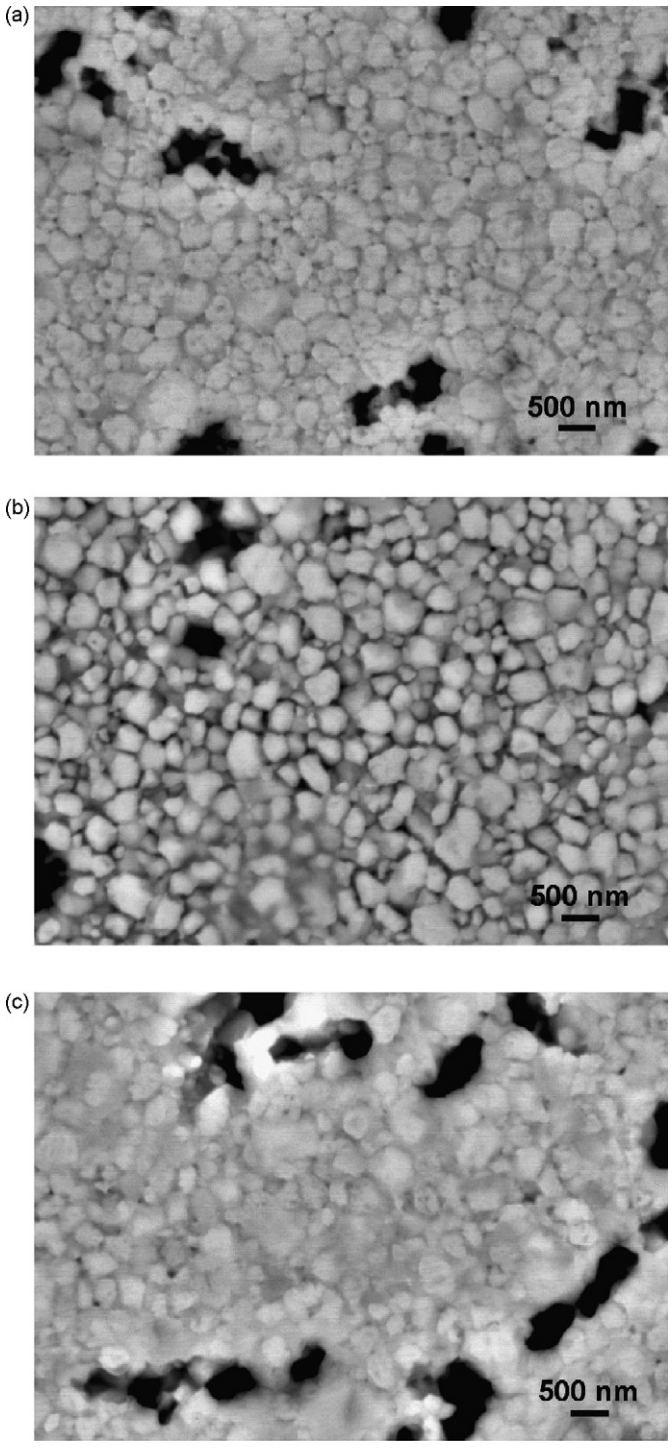

Fig. 6. Scanning electron micrographs of the sintered samples as a function of ball-milling time; (a) 12 h, (b) 24 h, (c) 48 h.

tives in different sizes were mixed as starting materials, it was somehow difficult to verify the change of powder particle size distribution through ball-milling from these SEM images. However, the sizes of more than 150 primary particles in SEM images were measured to give a result that D50 = 0.354 μm, 0.294 μm, 0.294 μm for 12 h, 24 h, 48 h milling, respectively. Another particle size measurement using PSA technique showed average values which are not quite different; D50 = 0.566 μm, 0.564 μm, 0.556 μm for 12 h, 24 h, 48 h milling (Fig. 2). Although this PSA measurement gives a larger value for average particle size mainly due to the agglomerated powders in the measurement, careful investigation of the PSA result revealed a slight increase of the number frequency of small sized powders as the milling time increased from 24 h to 48 h, which is marked by arrows in the figure inserted in Fig. 2. The results of particle size measurement using SEM and PSA indicated that 24 h milling reduced the primary powders compared to 12 h milling, and that the further increase in milling time to 48 h, induced comminution of raw powders which did not affect the overall particle size distribution. Unlike the size distribution, specific surface area (SSA) measurement of the milled powders showed the SSA value increasing in a linear proportion to the milling time; 4.583 m^2/g for 12 h, 5.931 m^2/g for 24 h, 9.191 m^2/g for 48 h milling, respectively. Considering the change of primary particle size measured from SEM images, the results of particle size and SSA measurements indicated that the systematic increase of specific surface area of milled powders resulted from additional factor as well as particle size reduction.

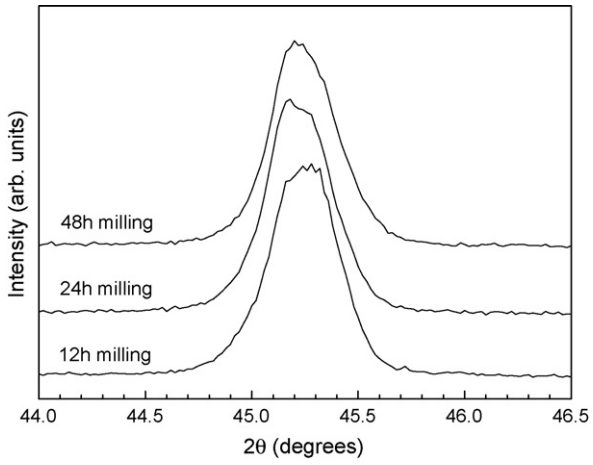

Fig. 7. XRD patterns of sintered samples as a function of milling time.

If the powder was subject to stress given by the milling process without any significant size reduction, then the residual strain of powder could be estimated by XRD or Raman spectroscopy. Fig. 3 shows XRD patterns of (0 0 2)/(2 0 0) and (1 1 3)/(3 1 1) peaks of the powders after ball-milling. As the milling time increased, the peak-to-peak separation was gradually degraded, which was attributed to the reduction of primary particle size. In addition, tetragonality of the powders determined using (0 0 2)/(2 0 0) peak positions also decreased; 1.0092 for 12 h, 1.0080 for 24 h, 1.0080 for 48 h milling. This indicates that the prolonged milling deteriorates the crystallinity of powders. The XRD peaks can be broadened by accumulated strain or size reduction of the diffracting particles in the specimen, and those effects can be estimated using the Hall–Williamson eq.,[15,16]

$$\left(\frac{B\cos\theta}{\lambda}\right)^2 = \left(\frac{0.89}{D}\right)^2 + 16\eta^2\left(\frac{\sin\theta}{\lambda}\right)^2 \quad (1)$$

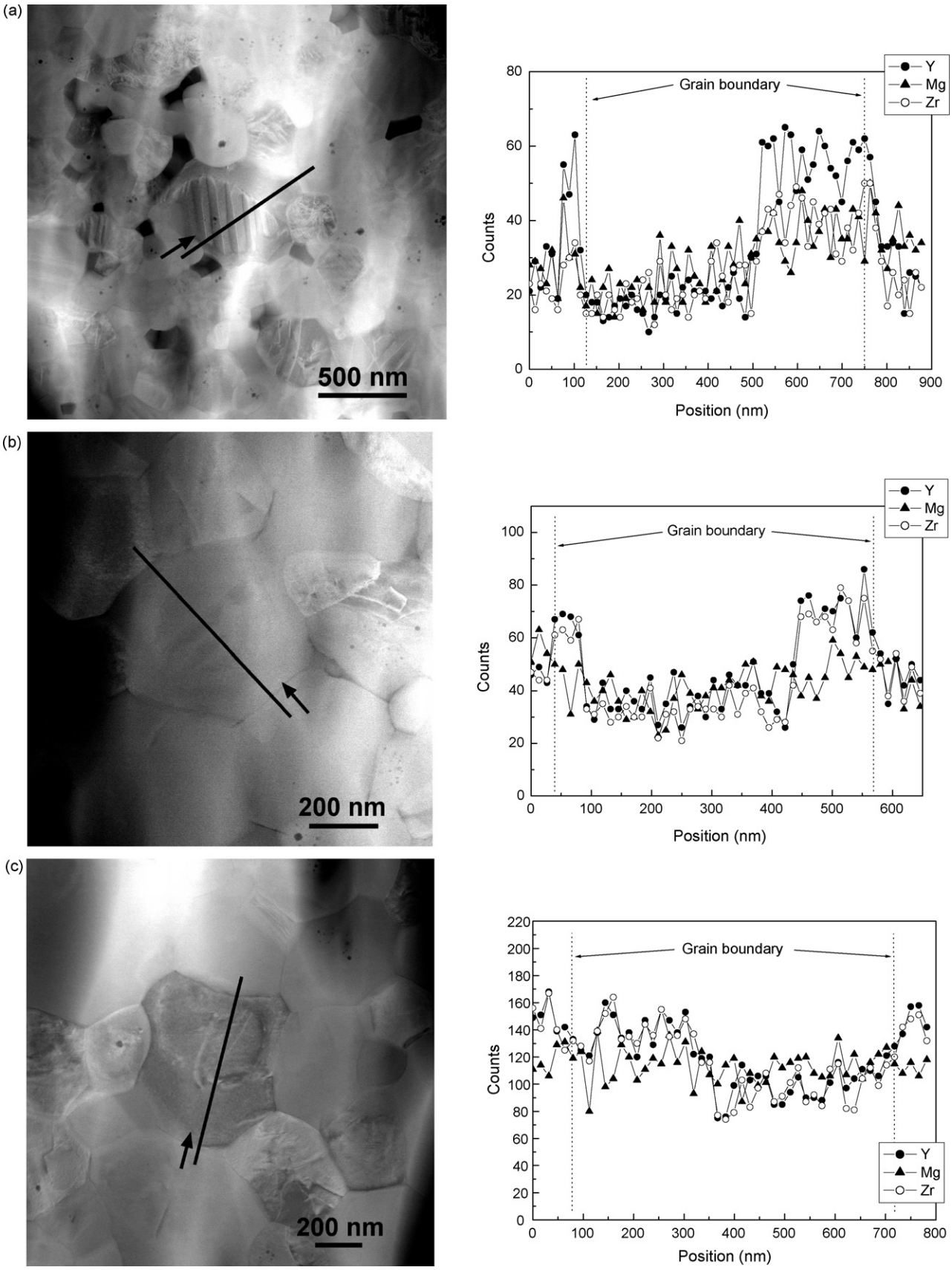

Fig. 8. Scanning transmission electron micrographs and EDS line profiles of typical core–shell grains in the specimen of (a) 12 h, (b) 24 h, (c) 48 h milling. (d) Bright field image of the grain in 48 h-milling specimen, showing extensive formation of shell up to 450 nm width.

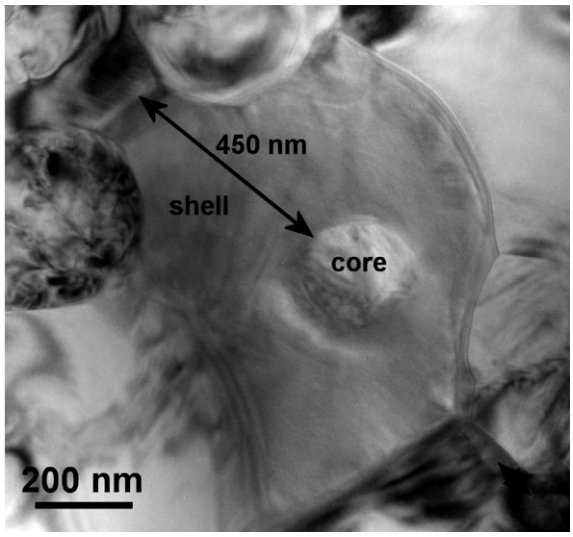

Fig. 8. (*Continued*).

where B is full-width-at-half-maximum (FWHM) of each XRD peak, θ Bragg angle, η residual strain, D particle size, λ wavelength of X-ray, and k equation constant, respectively. Plotting $(B\cos\theta/\lambda)^2$ vs. $(4\sin\theta/\lambda)^2$ with the values of Bragg angle and FWHM of each peak in the XRD pattern gives a value corresponding to strain from the slope and that corresponding to particle size from the intercept to Y-axis. To characterize the residual strain of powders, exclusive of the effects of additives, BT powders just added with sintering aids – SiO_2 and $BaCO_3$ – were ball-milled for a different time, in the same manner as for the powders with all additives. The Hall–Williamson plots determined from (0 0 1), (1 1 1), (2 0 0), (2 0 2), (2 2 2), and (4 0 0) peaks of each ball-milled powder are shown in Fig. 4. In spite of the scattering of data points, as the milling time increased, the linear fit of H-W plot became steeper, giving the strain value proportional to the milling time; 0.0010 for 12 h, 0.0012 for 24 h, and 0.0019 for 48 h, respectively.

The milled powders were also analyzed by Raman spectroscopy. For Raman spectroscopic study of BT, it is known that the peak of $A_1(TO_3)$ phonon mode located at about 516 cm^{-1} in the spectrum shifts to a higher wave number for the specimen subject to compressive strain and to a smaller value for tensile strain.[17] Therefore, to compare the amount of peak shift, 200 nm BT powders which were annealed at 1300 °C for 4 h, to sufficiently relieve any residual strain were scanned as a reference. Fig. 5(a) shows Raman spectra of BT powders milled for a different time. As in the XRD strain analysis, the amount of Raman peak shift with regard to the reference data was increased with increasing milling time. Fig. 5(b) shows that Raman peak shift corresponds linearly to the XRD strain. From the results of characterization of the milled powders, it is considered that the increase of ball-milling time from 12 h to 48 h, resulted in the accumulation of milling stress in the powders. In terms of powder size, however, it is considered that the increase of milling time from 12 h to 24 h, mainly reduced the primary powder size while the 48 h milling induced comminution of powders, not inducing any considerable change of overall size distribution. As a consequence, these changes of powder characteristics were expected to have an influence on the microstructure of the sintered specimen.

3.2. Characterization of sintered samples

The bulk density of the samples, which were formed with the previously described powders and sintered at 1350 °C, was almost unchanged; 5.87 g/cm^3 for 12 h, 5.82 g/cm^3 for 24 h, and 5.82 g/cm^3 for 48 h milling. And, the cross sectional SEM images of the chemically etched disks showed similar grain structures as shown in Fig. 6. The grain size distribution measured from the SEM images did not show any noticeable increase from the values of milled powders measured from SEM images; D50 = 0.349 μm for 12 h, 0.351 μm for 24 h, and 0.301 μm for 48 h milling.

The (0 0 2)/(2 0 0) XRD patterns of the sintered samples assumed pseudocubic peaks of a similar shape regardless of the milling time, as shown in Fig. 7. As described in our previous study, the formation of core–shell structure in the dielectric grains would change the XRD peak of bulk specimen from tetragonal to pseudocubic structure.[11] However, it is difficult to quantitatively deduce the variation of fractions of core (tetragonal) and shell (pseudocubic) from the change of XRD peak shape.

TEM investigation of each sample showed a general tendency that the core–shell grain in the sample with a longer milling time had a thicker shell, as shown in Fig. 8(a–c). And, in case of 48 h milling, a heavily formed shell was often observed in a fairly large grain (Fig. 8(d)), indicating the extensive shell formation in that sample. In order to estimate the extent of shell formation in the grain, it is more reasonable comparing the shell width to grain size ratio within a given grain rather than comparing the shell thickness of individual grains of different size. In the study of the effects of milling damage on the ceramic microstructure, Mizuno et al. observed about a hundred grains by TEM, classified them into core grain, shell grain and core–shell grain, then correlated the variation of the number frequency of each grain to the process condition.[13,14] However, compared to their approach, the investigation of the variation of shell portion in one core–shell grain seems to be able to reflect the effects of milling condition on the shell formation more reasonably. As a result, the grain size and shell width were measured for all core–shell grains observed in the TEM images of each sample, and the ratios of shell width to grain size were plotted in Fig. 9. Fig. 9 revealed that the shell portion in the dielectric grain tended to increase with the increasing milling time. This result could be understood based on that the increased milling time induces an increase in the residual strain and a size reduction of the powders, resulting in their surface activity enhanced, which in turn facilitates the reaction between the dielectric and additives during sintering to promote the shell formation. In addition, comminution of powders milled for 48 h, could also enhance the reaction of grain and additives, which sometimes induced an extensive formation of the shell as shown in Fig. 8(d). It is noted that though every core–shell grain showed slightly different concentration for shell composition, the shells observed in the sample with a

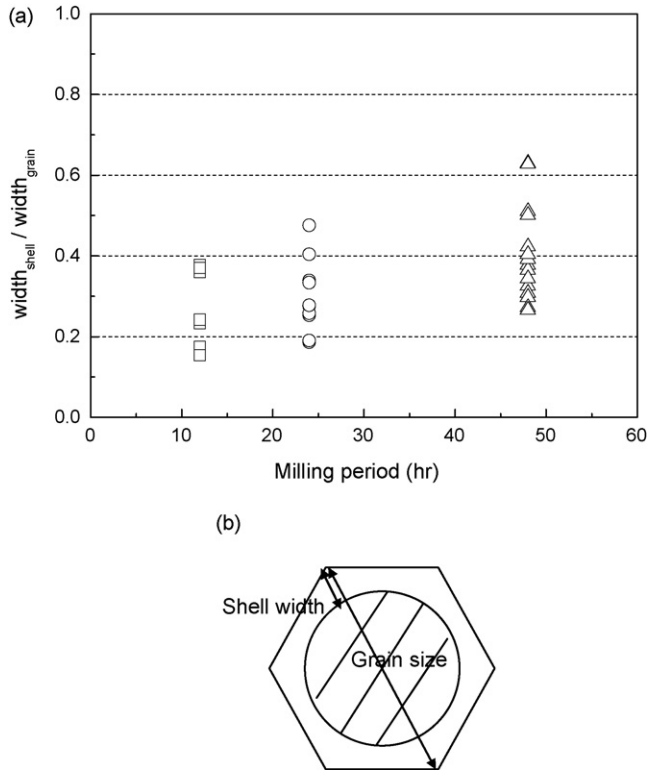

Fig. 9. (a) Plot of shell width to grain size ratio measured from TEM BF images as a function of milling time, (b) core–shell structure scheme for shell width to grain size ratio measurement.

longer milling time generally had an increased amount of Zr. This was attributed to the milling media remnant in the powders during the prolonged milling process. The Zr could function as a dopant in the shell formation, but since the main component in forming a shell is Y as reported in the previous study,[11] no further investigation on Zr in the shell was performed.

The increase in the shell portion observed in TEM investigation was confirmed by DCS analysis, as shown in Fig. 10. The area under the peak at about 125 °C corresponding to the latent heat of phase transition per unit mass decreased with

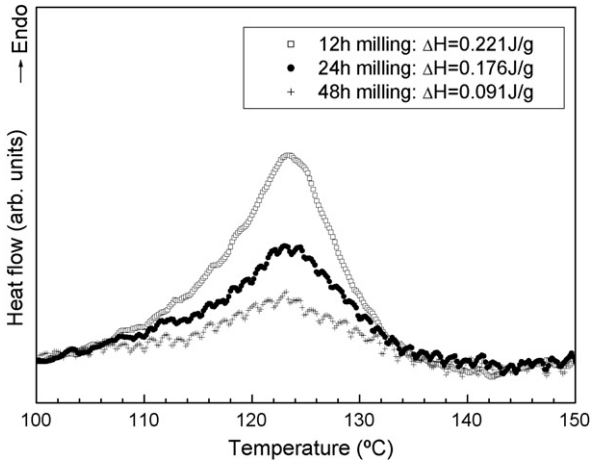

Fig. 10. Differential scanning calorimetry curves of sintered samples as a function of milling time.

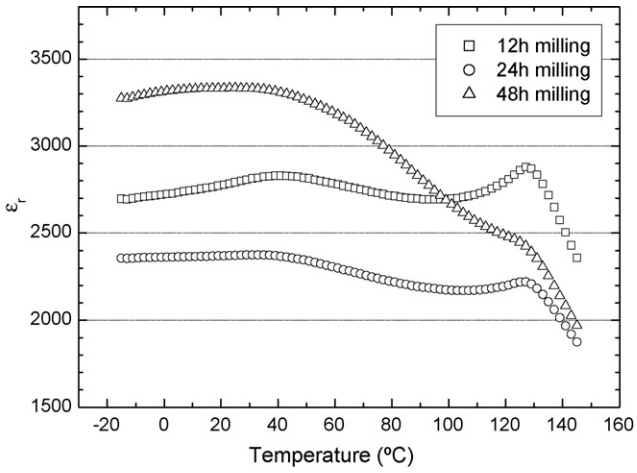

Fig. 11. Temperature dependence of relative dielectric constants of the samples as a function of milling time.

the increasing milling time, which is consistent with the TEM results showing the increased shell portion, i.e., the decreased core portion in the grains.

Fig. 11 shows temperature dependence of relative dielectric constants (ε_r's) of the sintered samples. When the milling time increased from 12 h to 24 h, ε_r was decreased over the whole measurement temperature range with the hot temperature end slightly more reduced. This behavior indicates the deteriorated dielectric property, and is attributed to the size reduction of primary powders. And, at 48 h milling, the low temperature part of the curve was appreciably raised up compared to the hot temperature end. For the core–shell structure, it is considered that the shell consists of a series of different phases according to their additive concentrations dissolved in BT lattice. These individual phases have their own Curie temperatures in ε_r–T curves, and the superposition of them results in rather diffuse ε_r–T curve. Consequently, the formation of shell could raise the low temperature part of ε_r–T curve, leading to the overall curve less temperature dependent.[18] It is reported that as the concentration of additive element in the shell region decreases, the diffuse phase transition temperature moves towards Curie temperature of pure BT.[19,20] It is also reported that in case of BT and additive powders which were ball-milled for a long time, the plot of capacitance change with temperature of the sintered ceramic sample had more negative ends on both of cold and hot temperature sides in spite of increased room temperature dielectric constant.[12] Therefore, the remarkable rise of low temperature part of ε_r–T curve of 48 h milling specimen was attributed to the prominent shell formation, as exemplified by the considerably thick shell width in Fig. 8(d), which resulted from comminution as well as accumulated stress on the milled powder.

4. Conclusions

To study the effects of ball-milling condition on the core–shell formation in BT grains, the powders ball-milled for a different time and the sintered specimen were investigated through various types of microstructural characterization techniques. As the milling time increased from 12 h to 48 h, the stress given by

the milling process was accumulated in the powders while the primary powder size was reduced at 24 h milling and additional comminution of powders occurred at 48 h milling. The change of powder characteristics did not induce any difference in the sinterability but influenced on the formation of core–shell structure in the sintered specimen. The increase in milling time facilitated the shell formation leading to the increased shell portion in the core–shell grain. Particularly at 48 h milling, the comminution effect as well as the increased milling stress resulted in the extensive formation of shell which was reflected by the remarkable rise of low temperature part of ε_r–T curve.

Acknowledgement

The authors are thankful to M. Park in Analytical Research Group at Samsung Electro-Mechanics for technical help in Raman spectroscopy measurement.

References

1. Rawal, B. S., Kahn, M. and Buessem, W. R., *Grain core-grain shell structure in barium titanate-based dielectrics. Advances in Ceramics*, *1*. The American Ceramic Society, Westerville, OH, 1981, pp. 172–188.
2. Hennings, D. and Rosenstein, G., Temperature-stable dielectrics based on chemically inhomogeneous $BaTiO_3$. *J. Am. Ceram. Soc.*, 1984, **67**, 249–254.
3. Randall, C. A., Wang, S. F., Laubscher, D., Dougherty, J. P. and Huebner, W., Structure property relationships in core-shell $BaTiO_3$-LiF ceramics. *J. Mater. Res.*, 1993, **8**, 871–879.
4. Yoon, S. H., Lee, J. H., Kim, D. Y. and Hwang, N. M., Core-shell structure of acceptor-rich, coarse barium titanate grains. *J. Am. Ceram. Soc.*, 2002, **85**, 3111–3113.
5. Armstrong, T. R. and Buchanan, R. C., Influence of core-shell grains on the internal stress state and permittivity response of zirconia-modified barium titanate. *J. Am. Ceram. Soc.*, 1990, **73**, 1268–1273.
6. Kishi, H., Okino, Y., Honda, M., Iguchi, Y., Imaeda, M., Takahashi, Y., Ohsato, H. and Okuda, T., The effect of MgO and rare-earth oxide on formation behavior of core-shell structure in $BaTiO_3$. *Jpn. J. Appl. Phys.*, 1997, **36**, 5954–5957.
7. Chazono, H. and Fujimoto, M., Sintering characteristics and formation mechanisms of core-shell structure in $BaTiO_3$-Nb_2O_5-Co_3O_5 ternary system. *Jpn. J. Appl. Phys.*, 1995, **34**, 5354–5359.
8. Chazono, H. and Kishi, H., Sintering characteristics in $BaTiO_3$-Nb_2O_5-Co_3O_4 ternary system: I, electrical properties and microstructure. *J. Am. Ceram. Soc.*, 1999, **82**, 2689–2697.
9. Fujikawa, Y., Umeda, Y. and Yamane, F., Analysis on the sintering process of X7R MLCC materials. *J. Jpn. Soc. Powder Powder Metall.*, 2004, **51**, 839–844.
10. Chen, C. S., Chou, C. C. and Lin, I. N., Microstructure of X7R type base-metal-electroded $BaTiO_3$ capacitor materials co-doped with MgO/Y_2O_3 additives. *J. Electroceram.*, 2004, **13**, 567–571.
11. Kim, C. H., Park, K. J., Yoon, Y. J., Hong, M. H., Hong, J. O. and Hur, K. H., Role of yttrium and magnesium in the formation of core-shell structure of $BaTiO_3$ grains in MLCC. *J. Eur. Ceram. Soc.*, 2008, **28**, 1213–1219.
12. Chu, M. S. H., Hodgkins, C. E. and Dean, T. C., Dielectric ceramic composition with high dielectric constant and flat TC characteristics. US Patent 4,882,305, 21 November 1989.
13. Mizuno, Y., Hagiwara, T., Chazono, H. and Kishi, H., Effect of milling process on core-shell microstructure and electrical properties for $BaTiO_3$-based Ni-MLCC. *J. Eur. Ceram. Soc.*, 2001, **21**, 1649–1652.
14. Mizuno, Y., Hagiwara, T., Kishi, H., Kirianov, A. and Ohsato, H., Influence of the milling process on microstructure and electrical properties for $BaTiO_3$-based Ni-MLCC. *J. Ceram. Soc. Jpn.*, 2004, **112**, S493–S497.
15. Williamson, G. K. and Hall, W. H., X-ray line broadening from filed aluminium and wolfram. *Acta Metall.*, 1953, **1**, 22–31.
16. Asiaie, R., Zhu, W., Akbar, S. A. and Dutta, P. K., Characterization of submicron particles of tetragonal $BaTiO_3$. *Chem. Mater.*, 1996, **8**, 226–234.
17. Dobal, P. S. and Katiyar, R. S., Studies on ferroelectric perovskites and Bi-layered compounds using micro-Raman spectroscopy. *J. Raman Spectrosc.*, 2002, **33**, 405–423.
18. Liu, X., Cheng, S. and Randall, C. A., The core-shell structure in ultrafine X7R dielectric ceramics. *J. Kor. Phys. Soc.*, 1998, **32**, S312–S315.
19. Feng, Q., McConville, C. J., Edwards, D. D., McCauley, D. E. and Chu, M., Effect of oxygen partial pressure on the dielectric properties and microstructures of cofired base-metal-electrode multilayer ceramic capacitors. *J. Am. Ceram. Soc.*, 2006, **89**, 894–901.
20. McCauley, D. E., Chu, M. S. H. and Megherhi, M. H., Po_2 dependence of the diffuse-phase transition in base metal capacitor dielectrics. *J. Am. Ceram. Soc.*, 2006, **89**, 193–201.